Hall Cascade with Fractional Magnetic Helicity in Neutron Star Crusts

Axel Brandenburg[1,2,3]
[1] Nordita, KTH Royal Institute of Technology and Stockholm University, Roslagstullsbacken 23, SE-10691 Stockholm, Sweden; brandenb@nordita.org
[2] Department of Astronomy, AlbaNova University Center, Stockholm University, SE-10691 Stockholm, Sweden
[3] McWilliams Center for Cosmology & Department of Physics, Carnegie Mellon University, Pittsburgh, PA 15213, USA

Abstract

The ohmic decay of magnetic fields in the crusts of neutron stars is generally believed to be governed by Hall drift, which leads to what is known as a Hall cascade. Here we show that helical and fractionally helical magnetic fields undergo strong inverse cascading like in magnetohydrodynamics (MHD), but the magnetic energy decays more slowly with time t: $\propto t^{-2/5}$ instead of $\propto t^{-2/3}$ in MHD. Even for a nonhelical magnetic field there is a certain degree of inverse cascading for sufficiently strong magnetic fields. The inertial range scaling with wavenumber k is compatible with earlier findings for the forced Hall cascade, i.e., proportional to $k^{-7/3}$, but in the decaying cases, the subinertial range spectrum steepens to a novel k^5 slope instead of the k^4 slope in MHD. The energy of the large-scale magnetic field can increase quadratically in time through inverse cascading. For helical fields, the energy dissipation is found to be inversely proportional to the large-scale magnetic field and proportional to the fifth power of the rms magnetic field. For neutron star conditions with an rms magnetic field of a few times 10^{14} G, the large-scale magnetic field might only be 10^{11} G, while still producing magnetic dissipation of 10^{33} erg s^{-1} for thousands of years, which could manifest itself through X-ray emission. Finally, it is shown that the conclusions from local unstratified models agree rather well with those from stratified models with boundaries.

Unified Astronomy Thesaurus concepts: Magnetohydrodynamical simulations (1966); Magnetars (992)

1. Introduction

Over the first hundreds of years after the freezing of the crust of a neutron star (NS), magnetic dissipation is believed to power the X-ray emission observed in the central compact objects of supernova remnants. At the same time, the large-scale magnetic field, as characterized by its dipole field strength, is not strong enough to explain this directly as a result of magnetic dissipation; see Gourgouliatos et al. (2016, 2018, 2020) for the motivation. Moreover, the magnetic field would decay too slowly to explain the observed emission. A plausible mechanism may therefore be the "turbulent" decay of a small-scale magnetic field in the NS's crust (Vainshtein et al. 2000). Such an enhanced decay with correspondingly enhanced Joule dissipation could be driven by the nonlinearity from the Hall effect (Hollerbach & Rüdiger 2002, 2004). Following Goldreich & Reisenegger (1992), we refer to this process simply as Hall cascade, keeping in mind that no motions are involved.

Traditionally, NS magnetic fields are explained as the result of compressive amplification of a large-scale magnetic field in the NS's progenitor. However, this explanation ignores the fact that the NS is fully convective during the first tens of seconds of its lifetime (Epstein 1979). Not only would this have destroyed a preexisting magnetic field, but it would have produced a potentially much stronger one from scratch (Thompson & Duncan 1993). Compared with the short timescales of such NS convection, the rotation is usually slow. It is therefore questionable whether this process alone could explain the large-scale magnetic field in supernova remnants. Instead, it is possible that the crust of the NS is dominated by a small-scale (turbulent) magnetic field at the time of freezing. However, rotation may still be responsible for causing the turbulence to be at least partially helical. This could be crucial for moderating the speed of the decay of the small-scale magnetic field. It could also explain the gradual amplification of a large-scale magnetic field through inverse cascading (Cho 2011).

In the NS crust, ions are immobile, so the electric current $\boldsymbol{J}$ is carried by the electrons alone. Their velocity is therefore $-\boldsymbol{J}/en_e$, where e is the elementary charge and n_e is the number density of electrons (see, e.g., Cho & Lazarian 2009). The evolution of the magnetic field $\boldsymbol{B}$ with time t is then given by

$$\frac{\partial \boldsymbol{B}}{\partial t} = \boldsymbol{\nabla} \times \left(-\frac{\boldsymbol{J} \times \boldsymbol{B}}{en_e} - \eta \mu_0 \boldsymbol{J} \right), \quad \boldsymbol{J} = \frac{1}{\mu_0} \boldsymbol{\nabla} \times \boldsymbol{B}, \quad (1)$$

where $\eta = 1/\mu_0 \sigma_{\rm el}$ is the magnetic diffusivity with μ_0 being the magnetic permeability, and $\sigma_{\rm el}$ is the electric conductivity. The nonlinearity in Equation (1) resembles that of the vorticity equation in hydrodynamics (Goldreich & Reisenegger 1992), although there are also significant differences. For example, Wareing & Hollerbach (2010) noted that, unlike usual turbulence, where smaller eddies are advected by larger ones, this is not the case in the Hall cascade. It is also known that the inertial range follows a $k^{-7/3}$ magnetic energy spectrum with wavenumber k (Biskamp et al. 1996, 1999), which is steeper than the Kolmogorov $k^{-5/3}$ kinetic energy spectrum.

Meanwhile, significant progress has been made in understanding the decay of hydrodynamic and magnetohydrodynamics (MHD) turbulence, both with and without magnetic helicity. The work of Brandenburg & Kahniashvili (2017) used the instantaneous scaling exponents p and q in the scalings of mean energy density $\mathcal{E} \propto t^{-p}$ and correlation length $\xi \propto t^q$ versus time t. They found that, as the solution approached self-similar scaling, p and q settled toward a specific point in a pq diagram. Particularly familiar cases are $p = 10/7$ and $q = 2/7$ when the Loitsiansky integral is conserved (Batchelor & Proudman 1956), $p = 6/5$ and $q = 2/5$ when the Saffman integral is conserved (Saffman 1967), or $p = q = 2/3$ when the magnetic helicity is conserved (Biskamp & Müller 1999).

In view of these new diagnostics, it is timely to revisit the evolution of magnetic fields in the Hall cascade.

In this paper, we study the initial value problem of Equation (1) for small-scale (turbulent) magnetic fields. Unlike Rheinhardt & Geppert (2002), who considered an initially large-scale magnetic field that becomes unstable and then leads to the production of small scales, we follow here the proposal of Goldreich & Reisenegger (1992) and consider the case of an initially small-scale field that continues to decay, but with the possibility of a nonvanishing magnetic helicity, which is a conserved quantity also in the Hall cascade (Cho 2011).

In addition to the turbulent conversion into Joule heat, we study the power-law decay of magnetic energy and of the peak wavenumber of the energy spectrum. We restrict ourselves to Cartesian geometry with coordinates $\boldsymbol{x} = (x, y, z)$. We focus on the case of triply periodic domains. This facilitates the use of Fourier spectra as our principal means of diagnostics and is best suited to address generic decay properties of the Hall cascade. However, to address the relevance of these idealized models to real NS crusts, we also consider stratified cases where the electron density and electric conductivity increase with height in an approximately realistic way. In those cases we use nonperiodic boundary conditions in the vertical direction. The use of standard three-dimensional Fourier transformation is then still possible, but as a diagnostic means it is not ideal unless Fourier transformation is only employed in the horizontal direction. We begin by presenting our basic model and study some of its relevant properties.

2. The Model

2.1. Units and NS Parameters

We consider a Hall cascade with a characteristic wavenumber k_0, which is where the spectrum peaks initially. It is related to the spherical harmonic degree ℓ, where most of the energy resides, through $k_0 = \ell/R$, where R is the NS radius. For reasons that will be given below, we will consider time-dependent values of η for many of our models. We therefore also define a representative constant η_0 that can be chosen to be equal to the initial value of η. In the stratified cases, the surface values of η and n_e are denoted by η_0 and n_{e0}, respectively. We present the results in nondimensional form by introducing the following units:

$$[\boldsymbol{x}] = k_0^{-1}, \quad [t] = (\eta_0 k_0^2)^{-1}, \quad [\boldsymbol{B}] = en_{e0}\mu_0\eta_0. \quad (2)$$

This implies that the current density is measured in units of $[\boldsymbol{J}] = [\boldsymbol{B}]\,k_0/\mu_0$. We will also be interested in the magnetic dissipation, $\epsilon = \eta\mu_0\langle\boldsymbol{J}^2\rangle$. It has dimensions of energy density per unit time, or $[\epsilon] = e^2 n_{e0}^2 \mu_0 \eta_0^3 k_0^2$.

Using $\mu_0 = 4\pi \times 10^{-7}$ T m A^{-1}, $e = 1.60 \times 10^{-19}$ As, $n_{e0} = 2.5 \times 10^{40}$ m^{-3}, and $\eta_0 = 4 \times 10^{-8}$ m^2 s^{-1} (Gourgouliatos et al. 2016, 2020), we have $[B] = 2 \times 10^{12}$ G, where 1 G $= 10^{-4}$ T has been used. With $\ell = 10$ (Gourgouliatos et al. 2016, 2020) and $R = 10^4$ m, we have $k_0 = 10^{-3}$ m^{-1}, so $[t] = 0.8$ Myr. We also have $[\epsilon] = 1.3 \times 10^9$ J m^{-3} s^{-1}. To obtain the total (electromagnetic and neutrino) luminosity L from Joule dissipation, we have to multiply ϵ by the volume, which we take to be 10^{12} m^3 for a 1 km thick layer around the NS. For the luminosity, we then find $[L] = 1.3 \times 10^{28}$ erg s^{-1}, where we have used 1 J $= 10^7$ erg. To express our simulation results in dimensionful units, we multiply by the appropriate units given above.

Before introducing fully nondimensional units in the next section, we point out that one could introduce a normalized magnetic field as $\boldsymbol{B}' = \boldsymbol{B}/en_e\mu_0$, which has dimensions of m^2 s^{-1}, i.e., the same as the magnetic diffusivity, and also the same as the velocity potential (scalar and vector). This is a natural choice, but it is somewhat unexpected given that in MHD one rather tends to think of the magnetic field as a velocity. This difference is significant in that it implies a dimensional argument for the resulting turbulence spectrum that is different from that in MHD. We return to this in Section 2.7.

2.2. The Basic Equation

In Equation (1), we replace $\boldsymbol{B} = \boldsymbol{B}'en_e\mu_0\eta_0$, to scale out both the Hall coefficient and η_0 in Equation (1); see, e.g., Rheinhardt & Geppert (2002). This implies that instead of varying the Hall coefficient, we study the behavior for different magnetic field strengths. For the rest of this paper, we drop the primes.

To preserve the solenoidality of the magnetic field at all times, it is convenient to solve the induction equation with the Hall term for the magnetic vector potential $\boldsymbol{A}$. In the unstratified case, we solve the equation

$$\frac{\partial\boldsymbol{A}}{\partial t} = -\boldsymbol{J}\times\boldsymbol{B} - \eta\boldsymbol{J} + \boldsymbol{f}, \quad \boldsymbol{J} = \boldsymbol{\nabla}\times\boldsymbol{B}, \quad (3)$$

where $\boldsymbol{B} = \boldsymbol{\nabla}\times\boldsymbol{A}$ is the magnetic field in terms of the magnetic vector potential, and $\boldsymbol{f}$ is a stochastic forcing function that is used in some our cases studied below. The minus sign in Equation (3) is insignificant and could have been scaled out as well.

In the stratified case, we choose the domain to be in the range $-d \leqslant z \leqslant 0$, where d is the depth and $z = 0$ is the position of the surface. We adopt the profile function $\zeta(z) = (1 - z/H_e)^4$ with $n_e \propto \zeta$ and $\eta \propto \zeta^{-2/3}$ (Gourgouliatos et al. 2016, 2020), where H_e is the scale height for the electron density and $\zeta = 1$ at the top. This formulation is accurate enough for the purpose of the present investigation, although more realistic profiles could be computed; see Chamel & Haensel (2008) for a review on the theory of the stratification of neutron star crusts. Instead of Equation (3), we now solve

$$\frac{\partial\boldsymbol{A}}{\partial t} = -\frac{\boldsymbol{J}\times\boldsymbol{B}}{\zeta} - \frac{\eta\boldsymbol{J}}{\zeta^{2/3}}, \quad (4)$$

and instead of periodic boundary conditions, we use a pseudo-vacuum condition ($\hat{\boldsymbol{z}}\times\boldsymbol{B} = 0$) on $z = 0$ and a perfect conductor condition ($\hat{\boldsymbol{z}}\times\boldsymbol{A} = 0$ with $\hat{\boldsymbol{z}}\cdot\boldsymbol{B} = 0$) on $z = -d$.

In the unstratified, triply periodic cases, we consider two types of initial fields: one with a broken power-law spectrum and one that is obtained by driving the system for a short amount of time with a monochromatic forcing. In the stratified case, we only consider a broken power-law spectrum without initial forcing, which is why we have omitted the $\boldsymbol{f}$ term in Equation (4). These procedures are described in the following two sections.

2.3. Broken Power-law Initial Conditions, $\boldsymbol{f} = 0$

As in Brandenburg & Kahniashvili (2017) and Brandenburg et al. (2017), we construct the initial condition for the magnetic

vector potential $A(x, 0)$ from a random three-dimensional vector field in real space that is δ-correlated in space. In the following, hats denote Fourier transformation in all three directions. We transform this field into Fourier space and construct the magnetic field as $\hat{B}(k) = ik \times \hat{A}(k)$. We then scale the magnetic field by a function of $k = |k|$ such that we obtain the desired initial spectrum. We also apply the projection operator $P_{ij} = \delta_{ij} - k_i k_j/k^2$ to make A divergence free, and add a certain fraction σ (not to be confused with the electric conductivity σ_{el}) to make the resulting field helical. Thus, we have

$$B_i(k) = B_0(P_{ij}(k) - i\sigma\epsilon_{ijl}k_l/k)g_j(k)S(k), \quad (5)$$

where $g_j(k)$ is the Fourier transform of a δ-correlated vector field in three dimensions with Gaussian fluctuations, k_0 is now identified with the initial wavenumber of the energy-carrying eddies, and $S(k)$ determines the spectral shape with (Brandenburg et al. 2017)

$$S(k) = \frac{k_0^{-3/2}(k/k_0)^{\alpha/2-1}}{[1 + (k/k_0)^{2(\alpha+7/3)}]^{1/4}}. \quad (6)$$

For a given value of B_0, the resulting initial value of the rms magnetic field B_{rms}, which will be denoted by $B_{rms}^{(0)}$, is usually somewhat larger. For $k_0/k_1 = 180$, for example, we find $B_{rms}^{(0)}/B_0 \approx 3.2$ when $\sigma = 0$, and $B_{rms}^{(0)}/B_0 \approx 4.5$ when $\sigma = 1$.

This broken power-law initial condition is also used in the stratified cases. The application of nonperiodic boundary conditions in the z direction may cause sharp gradients in places, but this never led to any noticeable effects.

2.4. Monochromatic Initial Driving, $f \neq 0$

In some cases, we apply in Equation (3) monochromatic forcing with the f term during a short initial time interval $0 \leqslant t \leqslant t_{ini}$ to produce an initial condition for the rest of the simulation, when $f = 0$. In some cases, when we are interested in stationary turbulence, we also keep $f \neq 0$ during the entire time of the simulation. When forcing is on, we select randomly at each time step a phase $-\pi < \varphi \leqslant \pi$ and the components of the wavevector k from many possible discrete wavevectors in a certain range around a given value k_0. In this way, the adopted forcing function

$$f(x, t) = \text{Re}\{\mathcal{N}\tilde{f}(k, t)\exp[ik \cdot x + i\varphi]\} \quad (7)$$

is white noise in time and consists of plane waves with average wavenumber k_0. Here, x is the position vector and $\mathcal{N} = [J][B](\eta_0 k_0^2 \delta t)^{1/2}$ is a normalization factor, where δt is the time step. The Fourier amplitudes are

$$\tilde{f}_i = (\delta_{ij} - i\sigma\epsilon_{ijl}k_l/k)\tilde{f}_j^{(0)}\left/\sqrt{1 + \sigma^2}\right., \quad (8)$$

where $\tilde{f}^{(0)}(k) = (k \times e)/[k^2 - (k \cdot e)^2]^{1/2}$ is a nonhelical forcing function. Here, e is an arbitrary unit vector that is not aligned with k. Note that $|f|^2 = 1$. We consider both $\sigma = 0$ and $\sigma = 1$, corresponding to nonhelical and maximally helical cases. The forcing is only enabled during the time interval $0 \leqslant t \leqslant t_1$, where t_1 is the actual starting time of the simulation. In this sense, this forcing procedure can be considered as part of the initial condition.

2.5. Spectral Diagnostics

In the triply periodic cases, we study the evolution of magnetic energy and magnetic helicity spectra, which are defined as (see Brandenburg & Nordlund 2011)

$$E(k) = \frac{1}{2}\sum_{k_-<|k|\leqslant k_+}|\hat{B}(k)|^2, \quad H(k) = \text{Re}\sum_{k_-<|k|\leqslant k_+}\hat{A} \cdot \hat{B}^*, \quad (9)$$

where $k_\pm = k \pm \delta k/2$ and $\delta k = 2\pi/d$ is the wavenumber increment and also the smallest wavenumber

$$k_1 \equiv \delta k = 2\pi/d \quad (10)$$

in our cube of side length d. The helicity spectrum $H(k)$ is not to be confused with the electron scale height H_e. We also compute the corresponding magnetic energy and helicity transfer spectra (Rempel 2014)

$$T_E(k) = -\text{Re}\sum_{k_-<|k|\leqslant k_+}\hat{J}_k \cdot \widehat{(J \times B)}_k^*, \quad (11)$$

$$T_H(k) = -\text{Re}\sum_{k_-<|k|\leqslant k_+}\hat{B}_k \cdot \widehat{(J \times B)}_k^*. \quad (12)$$

In the case when $f \neq 0$, there are also source terms $S_E(k)$ and $S_H(k)$ that are defined analogously to $T_E(k)$ and $T_H(k)$, but with $J \times B$ being replaced by f. The magnetic energy and helicity spectra then obey

$$\frac{\partial}{\partial t}E(k, t) = 2T_E(k, t) - 2\eta k^2 E(k, t) + 2S_E(k, t), \quad (13)$$

$$\frac{\partial}{\partial t}H(k, t) = 2T_H(k, t) - 2\eta k^2 H(k, t) + 2S_H(k, t). \quad (14)$$

The mean magnetic energy and helicity densities are defined as $\mathcal{E} = \langle B^2 \rangle/2$ and $\mathcal{H} = \langle A \cdot B \rangle$ in terms of the magnetic energy and helicity spectra as

$$\int E(k, t)dk = \mathcal{E}(t), \quad \int H(k, t)dk = \mathcal{H}(t). \quad (15)$$

The rms magnetic field can be obtained through $B_{rms} = (2\mathcal{E})^{1/2}$. We define the magnetic correlation length ξ as

$$\xi(t) = \int k^{-1}E(k, t)dk \left/ \int E(k, t)dk\right.. \quad (16)$$

We define the instantaneous exponents describing the growth of $\xi(t)$ and the decay of $\mathcal{E}(t)$ as

$$q(t) = d\ln\xi/d\ln t, \quad p(t) = -d\ln\mathcal{E}/d\ln t. \quad (17)$$

Those play important roles in describing the nature of the turbulence in different cases (see Brandenburg & Kahniashvili 2017). To quantify inverse cascading, we use a variable similar to p, but now for the large-scale magnetic field only. Because we expect the magnetic field to increase at large scales, it will be defined with a plus sign, i.e.,

$$p_{LS}(t) = d\ln\mathcal{E}_{LS}/d\ln t, \quad (18)$$

where $\mathcal{E}_{LS}(t) = \int_{k_1}^{3k_1} E(k, t)dk$, which is an arbitrarily chosen compromise between relying only on a single wavenumber (just k_1) and some other weighted average that takes the entire spectrum into account, but emphasizes the low wavenumbers.

2.6. Invariance Under Rescaling

In connection with decaying hydrodynamic and MHD turbulence studies, Olesen (1997) was the first to make use of the invariance of the MHD equations under rescaling of space and time coordinates, along with a corresponding rescaling of the other dependent variables. A similar procedure applies analogously to Equation (3), which is invariant under the following rescaling:

$$t = \tau t', \quad \mathbf{x} = \tau^q \mathbf{x}', \quad \eta = \tau^{2q-1}\eta',$$
$$\mathbf{A} = \tau^{3q-1}\mathbf{A}', \quad \mathbf{B} = \tau^{2q-1}\mathbf{B}', \quad \mathbf{J} = \tau^{q-1}\mathbf{J}'. \quad (19)$$

Inserting these variables into Equation (3), the resulting equation in the primed quantities has the same form as Equation (3) in its original formulation. This requires that $\eta \propto t^r$ where $r = 2q - 1$. For $q < 1/2$, r is negative so t^r becomes singular for $t \to 0$. Therefore, we use in such cases

$$\eta(t) = \eta_0[\max(1, t/t_0)]^r, \quad (20)$$

where t_0 is the time below which η is assumed fixed.

It should be noted that the scaling in Equation (19) is different from that found in MHD, where, ignoring the density factor, $[\mathbf{B}] = [\mathbf{x}]/[t] \propto \tau^{q-1}$. This difference is significant and results in new relationships between p and q. We return to this in the next section.

In view of the limited dynamical range available in numerical simulations of decaying turbulence, the use of a time-dependent η implies significant computational advantages in that a suitably defined Lundquist number is then approximately constant over much of the duration of the run. It allows us to identify self-similar scaling properties. In particular, since both B_{rms} and η decay in time, we can characterize a "typical" B_{rms} by specifying the temporal average of their normalized ratio, namely

$$\tilde{B}_{rms} \equiv \langle B_{rms}/(en_e\mu_0\eta)\rangle. \quad (21)$$

Similarly, the magnetic dissipation can be expressed in a similar fashion as

$$\tilde{\epsilon} \equiv \langle \epsilon/(e^2n_e^2\mu_0\eta^3/\xi^2)\rangle, \quad (22)$$

where not only η decreases, but ξ increases such that the normalization factor of ϵ decreases in a similar fashion. Furthermore, since ξ increases with time, the averaged ratio

$$\tilde{\eta} \equiv \langle t\eta/\xi^2\rangle \quad (23)$$

is another quantity that we quote for our runs to characterize the effective value of η.

The definitions of $\tilde{B}_{rms}$, $\tilde{\epsilon}$, and $\tilde{\eta}$ remain somewhat problematic in that they are averages over ratios that can still show a residual trend, so the result depends on the time interval of averaging. However, for the purpose of this paper, we only want to provide a first orientation. We should keep this caveat in mind when those values are quoted below.

2.7. Dimensional Argument for Inertial Range Scaling

Biskamp et al. (1996) where the first to suggest a $k^{-7/3}$ inertial range spectrum scaling based on an energy transfer rate proportional to the cube of the electron velocity potential. Wareing & Hollerbach (2009) proposed a slightly different scaling proportional to $k^{-5/2}$, but did not suggest any phenomenology for that. It is clear that dimensional arguments

cannot emerge when one expresses the magnetic field in velocity units, as is usually done in MHD (see also Cho & Lazarian 2009). A physically more meaningful normalization for the Hall cascade is in terms of diffusivity units by noting that $\mathbf{B}/en_e\mu_0$ (where $\mathbf{B}$ is here in Tesla) has dimensions of $\mathrm{m^2\,s^{-1}}$. In those units, $E(k)$ has dimensions $\mathrm{m^5\,s^{-2}}$, and ϵ has dimensions $\mathrm{m^4\,s^{-3}}$. Making the ansatz

$$E(k) = C_{Hall}\,\epsilon^a k^b \quad (24)$$

with exponents a and b and the dimensionless coefficient C_{Hall}, we find, on dimensional grounds, $a = 2/3$ and $b = -7/3$, which is consistent with the result of Biskamp et al. (1996), although the coefficient C_{Hall} has not previously been introduced in this form, nor have estimates for its value been provided. Results for C_{Hall} will be given below, separately for helical and nonhelical turbulence.

In the time-dependent case, given that $E(k, t)$ has now different dimensions than in MHD, we have to adapt the corresponding arguments of Olesen (1997) and Brandenburg & Kahniashvili (2017) for self-similar solutions. If solutions are self-similar, the simultaneous dependence on k and t can be captured by a function ϕ, which depends only on the scaled wavenumber $k\xi(t)$, such that the peak of the spectrum is always at $k\xi(t) \approx 1$. In addition, the decrease of the amplitude of the spectrum with time is compensated by the prefactor $\xi^{-\beta}$ with some exponent β, so we have

$$E(k\xi(t), t) = \xi^{-\beta}\phi(k\xi). \quad (25)$$

We must require E itself to be invariant under rescaling,

$$E \to E'\tau^{5q-2} \propto \xi^{-\beta}\tau^{-\beta q}\phi(k\xi), \quad (26)$$

so we must require that $5q - 2 = -\beta q$, and therefore we have $\beta = 2/q - 5$. This relation is similar to that in MHD, except that the 5 is then replaced by 3.

Let us relate this now to the decay law for energy, which is of the form $\mathcal{E} \propto t^{-p}$. Since

$$\mathcal{E}(t) = \int E(k, t)dk \propto \xi^{-\beta}, \quad (27)$$

and using $\xi \propto t^q$, we have $p = (1 + \beta)q$, just like in MHD; see Equation (6) of Brandenburg & Kahniashvili (2017). This implies that, in the pq diagram, self-similar solutions must lie on the line

$$p = 2(1 - 2q) \quad \text{(selfsimilarity line)}, \quad (28)$$

which is steeper than the corresponding line $p = 2(1 - q)$ in MHD.

As in MHD, the relevant values of β and q depend on the physics governing the decay. If the decay is governed by magnetic helicity (Cho 2011), which has now dimensions $[x]^5/[t]^2$, then $q = 2/5$ and $\beta = 0$. Whether or not there can be other relevant quantities in the nonhelical case analogous to the Loitsiansky integral ($\beta = 4$) or the Saffman integral ($\beta = 2$) is unclear. In MHD, the case $\beta = 1$ has been associated with the possibility that some locally projected squared vector potential, $A_{\perp}^2$, may be conserved (Brandenburg et al. 2015). Some of our simulations point to a possible relevance of lines with $\beta = 2$–3 in the pq diagram. In Table 1 we summarize the other associated coefficients for several values of β.

The result $\mathcal{E} \propto \xi^{-\beta}$ in Equation (27) is a consequence of integrating $\phi(k\xi)$ over all $k\xi$, which gives just a number,

Table 1
Self-similarity Parameters for Different Values of β

β	q	p	r	comment
0	$2/5 = 0.40$	$2/5 = 0.40$	-0.20	$\langle \boldsymbol{A} \cdot \boldsymbol{B} \rangle = $ const
1	$2/6 = 0.33$	$4/6 = 0.86$	-0.33	$\langle A_\perp^2 \rangle = $ const ?
2	$2/7 = 0.29$	$6/7 = 0.86$	-0.43	Saffman-type scaling
3	$2/8 = 0.25$	$8/8 = 1.00$	-0.50	
4	$2/9 = 0.22$	$10/9 = 1.11$	-0.56	Loitsiansky-type scaling

Note. The question mark indicates uncertainty in the statement.

leaving only $\xi^{-\beta}$ outside the integral. In the calculation of $\mathcal{E}_{\rm LS}$, however, only a fixed k range matters, so the result depends on the slope of α of the subinertial range and the slope β of the envelope, and therefore we expect $p_{\rm LS} = (\alpha - \beta)q$. Using $\beta = 2/q - 5$ and $\alpha = 5$ (see below), this gives $p_{\rm LS} = 10q - 2$. For the helical case with $q = 2/5$, we therefore expect $p_{\rm LS} = 2$.

2.8. Numerical Simulations

For our numerical simulations we use the PENCIL CODE (https://github.com/pencil-code), which is a public MHD code that is particularly well suited for simulating turbulence. In practice, both B_0 and η_0 were varied, but the decisive control parameter is just a ratio $B_0/en_e\mu_0\eta$. However, in all the tables and plots presented below, we express the results in normalized form. The numerical resolution is 1024^3 mesh points in most of the cases presented below. A summary of all simulations is given in Tables 2 and 3. Here, t_2 denotes the end time of the simulation. In Runs A–F, the start time is $t = 0$, but our data analysis commences at $t=t_1$. The different values of t_2 are partly explained by the different speeds at which ξ grows and also the different numerical time steps, making runs with stronger magnetic field less economic to run. We usually spend 1–7 days per run on 1024 processors on a Cray XC40, where a time step takes about 0.4 s. The run directories for simulations are publicly available; see Brandenburg (2020a).

3. Results

3.1. Inertial Range for the Stationary Case

We begin by making contact with previous work and verify that the expected $k^{-7/3}$ inertial range scaling is obtained in the stationary case. To simulate this, we invoke the forcing term $\boldsymbol{f}$ during the entire time of the simulation. We choose $k_0 = 2k_1$. The resulting spectra, compensated by $\epsilon^{-2/3}k^{7/3}$, are shown in Figure 1 for nonhelical and helical forcings. Note that the $k^{-7/3}$ scaling is reproduced in both cases. Furthermore, there is no (or not the usual) diffusive subrange. The lack of a diffusive subrange was already emphasized by Wareing & Hollerbach (2010), which they ascribed to nonlocal spectral energy transfer. This lack of a diffusive subrange is related to the fact that the highest derivative in the linear and nonlinear terms in Equations (3) and (4) is the same, i.e., both terms are proportional to $\boldsymbol{J}$. Earlier simulations (Biskamp et al. 1996, 1999; Cho & Lazarian 2004) used hyperviscosity, which leads to an artificial dissipative cutoff, precluding any statements about a naturally occurring cutoff.

By compensating the spectra with $\epsilon^{-2/3}k^{7/3}$, the value of $C_{\rm Hall}$ in Equation (24) can be read off from Figure 1 as the height of the plateau. We find $C_{\rm Hall} \approx 2.7$ in the nonhelical

case (Run II) and $C_{\rm Hall} \approx 1.6$ in the helical case (Run III); see Table 3. For Run I with stronger forcing, however, we find $C_{\rm Hall} \approx 2.7$, but this could be because the resulting magnetic field strength is here too large for the numerical resolution, so the value of ϵ could be underestimated and therefore the compensated value appears too large. Note also that $T_E(k)$ has been scaled by $\eta_0^{-1}\epsilon^{-2/3}k^{1/3}$, which allows us to see that Equation (13) is approximately obeyed. In the helical cases, the current helicity displays a forward cascade (Brandenburg & Subramanian 2005). We therefore write $k^2H(k, t) = C_{\rm Hall}^{\rm hel}\epsilon_{\rm H}^{2/3}k^{-2}$, which follows from dimensional arguments analogous to those for $E(k, t)$. Here, $C_{\rm Hall}^{\rm hel}$ is a new coefficient and $\epsilon_{\rm H} = 2\eta \int k^2H(k, t)dk$ is the magnetic helicity dissipation. However, our simulation results for $k^4H(k, t)$ do not show a plateau, so we refrain here from pursuing this question further.

3.2. Nonhelical Decay

We now consider a nonhelical initial magnetic field. The case where an initial magnetic field is obtained via short-term monochromatic driving is shown in Figure 2, where we present the resulting spectra at different times. To see whether the magnetic helicity plays a role in our simulations, we plot $|kH(k, t)/2|$ together with $E(k, t)$. This representation is useful because of the realizability condition, which states that

$$|kH(k, t)/2| \leqslant E(k, t), \quad (29)$$

so we see immediately at which wavenumbers the inequality is closest to saturation. Since $H(k, t)$ can have either sign, we use red (blue) symbols to indicate positive (negative) values. We see that, at early times, $|kH(k, t)/2|$ is much smaller than $E(k, t)$. This changes at later times after $E(k, t)$ has dropped by several orders of magnitude. It is possible that the realizability condition limits further decay of $E(k, t)$, even though $H(k, t)$ does not have a definite sign.

By comparison, the case with an initial power-law spectrum is shown in Figure 3 for weak and strong magnetic fields. It turns out that, depending on the strength of the initial magnetic field, there is always a certain amount of inverse transfer, i.e., the spectral energy increases with time at small k, so $p_{\rm LS} > 0$. This confirms earlier findings by Cho & Lazarian (2009), Wareing & Hollerbach (2009), and Cho (2011).

In Figure 4 we show the pq diagram for Run A. Note the convergence of the point (p, q) toward the self-similarity line with $p \approx 0.9$ and $q \approx 0.3$. We have chosen to plot $p_{\rm LS}$ in the same plot, although it reflects different physics not related to β. It simply allows us to obtain a visual impression of how $p_{\rm LS}$ changes. In the present case, we see that $p_{\rm LS}$ approaches the value 0.5.

3.3. Approach to k^5 Scaling

Our initial conditions usually have a k^4 subinertial range spectrum. In the cosmological context, such a spectrum is motivated by causality requirements for early times (Durrer & Caprini 2003). It follows from a δ-correlated magnetic vector potential, so the shell-integrated spectrum of A corresponds to that of white noise and that of B corresponds to that of blue noise.

Looking at Figure 3(b), we see that the k^4 spectrum gradually evolves toward k^5. This steepening is rather remarkable and has

Table 2
Parameters for the Unstratified Models

Run	f_0	$B_0/[B]$	$B_{rms}^{(0)}/[B]$	σ_0	$-r$	k_0/k_1	$t_1/[t]$	$t_2/[t]$	$\tilde{\eta}$	$\tilde{B}_{rms}$	$\tilde{\epsilon}$	p_{LS}	p	q	Comment
A	0	200	600	0	0.43	180	0.2	4600	0.13	80	2×10^4	0.5	0.9	0.3	$\beta = 3 \rightarrow 2$
B	0	2000	6000	0	0.43	180	0.1	500	0.024	600	3×10^6	1.4	0.8	0.3	$\beta \approx 2$
C	0	2000	6000	10^{-3}	0.43	180	0.1	1000	0.020	800	6×10^6	1.5	0.4	0.4	$\beta = 2 \rightarrow 0$
C'	0	3000	10000	10^{-3}	0.20	180	0.1	100	0.040	300	5×10^5	1.8	0.5	0.4	$\beta = 2 \rightarrow 0$
D	0	2000	6000	10^{-2}	0.43	180	0.1	50	0.012	1500	3×10^7	2.5	0.4	0.4	$\beta = 2 \rightarrow 0$
E	0	2000	8000	1	0.43	180	0.001	10	0.003	6000	2×10^8	2.5	0.4	0.4	$\beta = 0$
F	0	200	1000	1	0	180	0.01	16	0.02	1000	6×10^6	1.3	0.6	0.3	$\beta = 0$
a	4×10^{-4}	150	350	0	0.43	60	0.02	1800	0.09	130	7×10^4	0.8	0.9	0.3	$\beta \approx 2$
b	4×10^{-3}	1500	3500	0	0.43	60	0.02	75	0.015	1100	1×10^7	1.3	1.0	0.3	$\beta \approx 2$
c	3×10^{-2}	1500	4000	1	0.43	60	0.02	4	0.004	5000	2×10^8	2.2	0.4	0.4	$\beta = 0$

Note. The resolution is 1024^3 mesh points for Runs A–F and 512^3 mesh points for Runs a–c.

Table 3
Model Parameters for Stationary Turbulence

Run	f_0	σ_0	$\tilde{B}_{rms}$	$\tilde{\epsilon}_{rms}$	C_{Hall}
I	4×10^{-2}	0	1450	15×10^7	4.5
II	4×10^{-3}	0	300	2×10^6	2.7
III	4×10^{-3}	1	360	7×10^5	1.6

Note. The resolution is 512^3 mesh points and $k_0/k_1 = 2$ in all three cases.
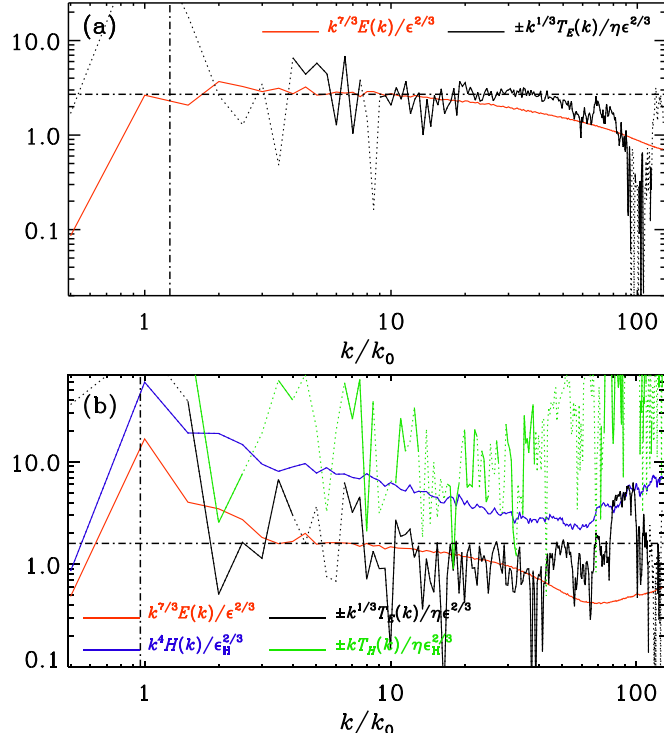

Figure 1. Stationary Hall cascade for Run II without helicity (a) and Run III with helicity (b). Solid (dotted) parts of the lines denote positive (negative) values.

Figure 2. $E(k, t)$ (solid black lines) and $H(k, t)$ (dotted lines) with positive (negative) values indicated by red (blue) closed (open) symbols for the nonhelical Runs a and b. The vertical dashed–dotted lines show the positions where $k\xi = 1$.

never been seen in MHD. In MHD, by contrast, it is known that, in the presence of magnetic helicity, a shallower initial spectrum involves gradually toward a k^4 spectrum; see Figure 3(a) of Brandenburg & Kahniashvili (2017).

Inverse transfer, on the other hand, has been seen in nonhelical MHD with strong magnetic fields (Brandenburg et al. 2015),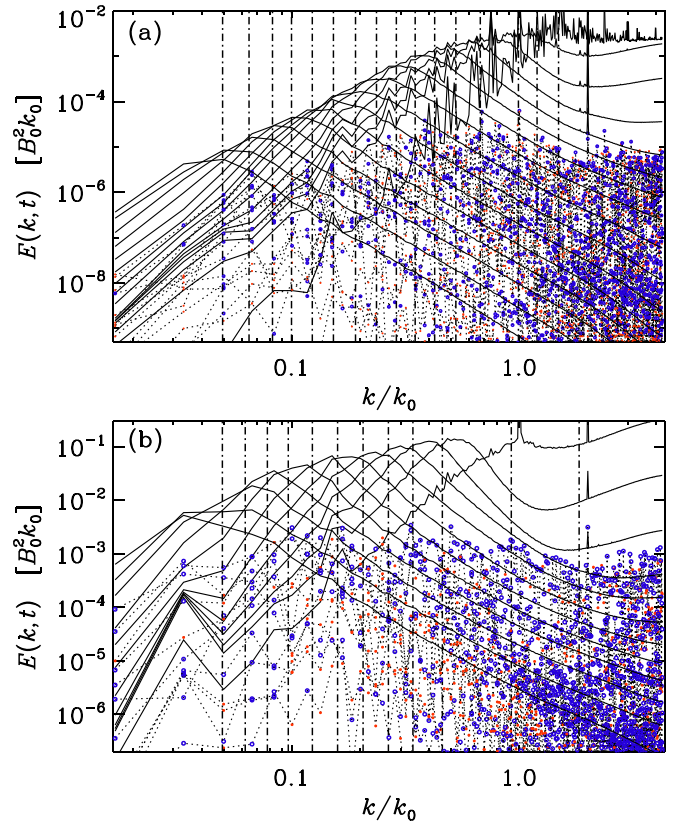 but here the effect is much more pronounced. This can be qualitatively explained by the nonlinearity of Equation (3), because we have seen that the nonhelical inverse transfer is stronger for a stronger magnetic fields. Therefore, the peak of the magnetic energy spectrum, where the field is stronger, is expected to move faster toward lower wavenumbers than the lower parts where the field is weaker. This is seen in Figure 3(a), where the magnetic field is weaker and the spectrum remains somewhat shallower than k^5.

3.4. Fully Helical Initial Fields

Next, we demonstrate the effect of finite magnetic helicity. It is well known that its presence constrains the mean magnetic
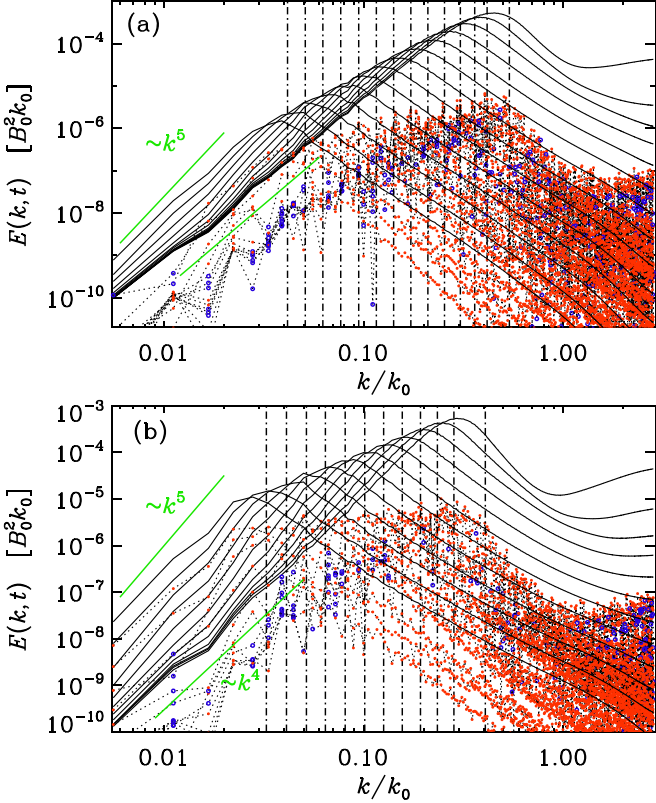
Figure 3. Similarly to Figure 2, but for (a) Run A and (b) Run B with weak and strong fields.
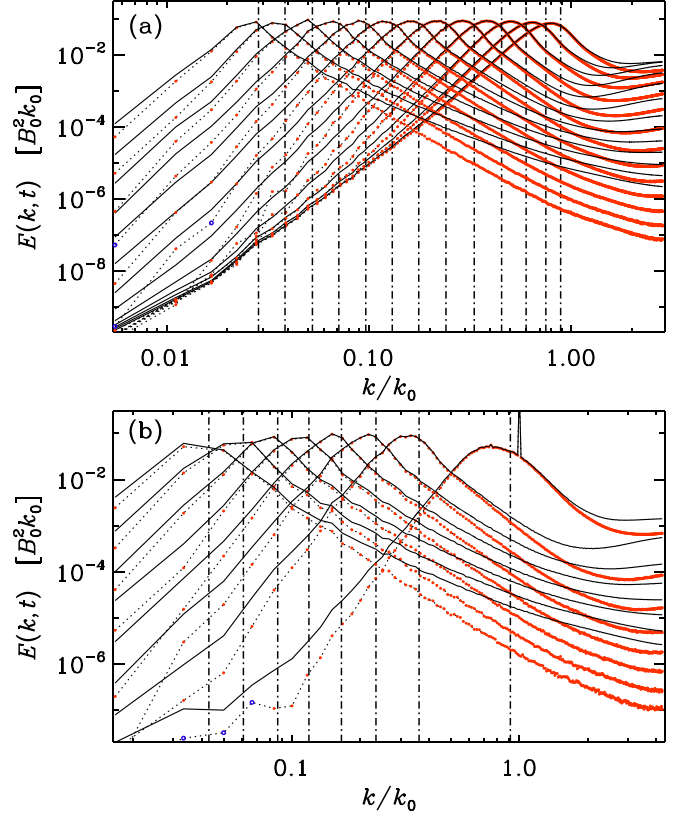

Figure 5. Similar to Figure 2, but for (a) Run E and (b) Run c, which have different initial conditions, but are both fully helical.
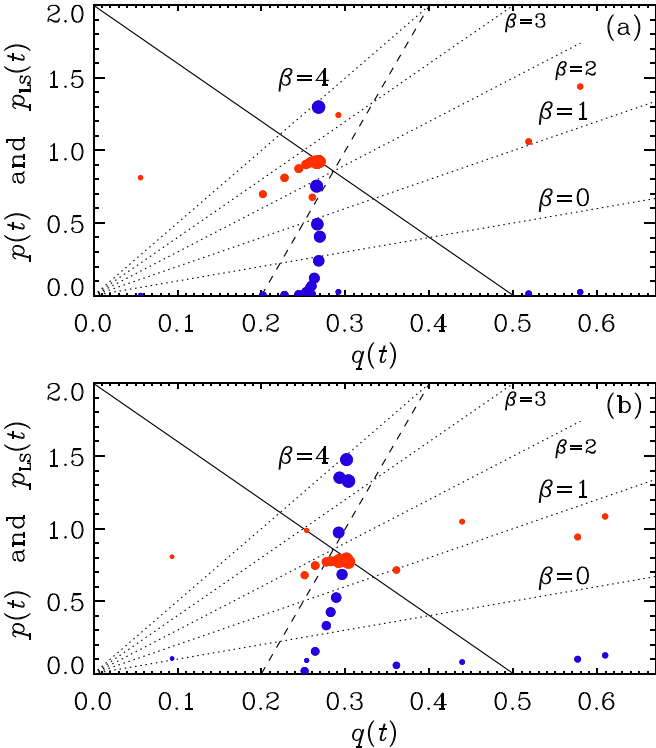

Figure 4. pq diagram showing p (red symbols) and p_{LS} (blue symbols) vs. q for Runs A and B in panels (a) and (b), respectively. Larger symbols indicate later times. The self-similarity line (solid) and the $p_{LS} = 10q - 2$ line (dashed) of Section 2.7 are also shown.
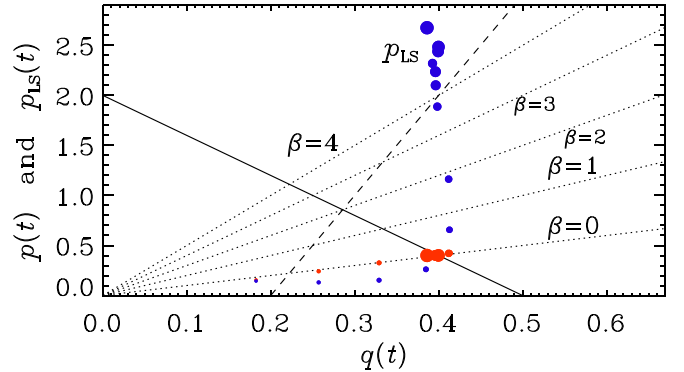
Figure 6. Similar to Figure 4, but for Run E.

energy density from below, so that

$$\mathcal{E}(t) \geqslant |\mathcal{H}|/2\xi(t), \tag{30}$$

which is similar to the spectral realizability condition mentioned above. Since $\mathcal{H}$ is nearly constant, $\mathcal{E}(t)$ can only decrease if $\xi(t)$ increases at the same rate, and therefore $p = q$.

In Figure 5 we plot $E(k, t)$ at times separated by a factor of $10^{1/3} \approx 2.15$. We also plot the normalized helicity, $kH(k, t)/2$. We see that it quickly begins to evolve underneath a flat envelope. Note that the amplitude of the spectrum is unchanged with time, so the exponent β in Equation (25) must be zero. The same behavior is seen in a case where the initial spectrum is driven by short-term forcing; see Figure 5(b). In the pq
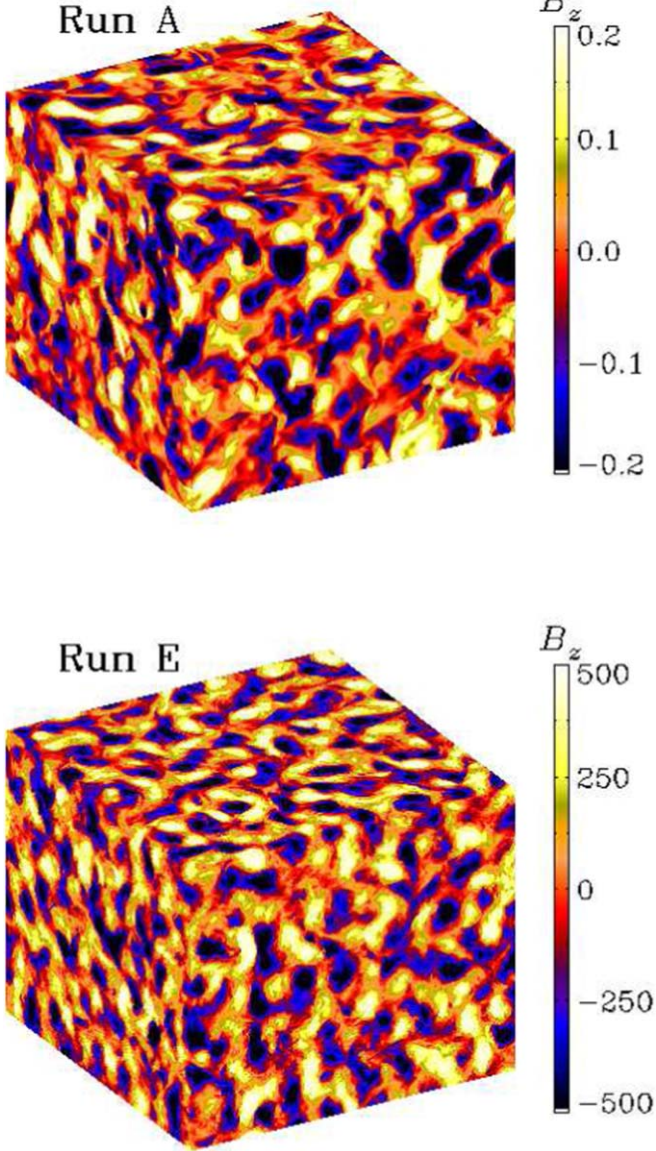
Figure 7. Visualization of B_z on the periphery of the computational domain for Runs A and E at a time when $k_0 \xi(t) \approx 24$.

Figure 8. (a) Magnetic energy spectrum (red) and scaled magnetic helicity spectrum (blue), and (b) the corresponding transfer spectra of magnetic energy and scaled magnetic helicity for Run A. Solid (dotted) line sections denote positive (negative) values.

Figure 9. Same as Figure 8, but for Run E.

diagram, the solution displays a drift of the point (p, q) along the $\beta = 0$ line toward the point $p = q = 2/5$; see Figure 6.

In Figure 7 we show visualizations of B_z on the periphery of the computational domain for Runs A and E. Both figures look remarkably similar, so the presence of helicity bears no obvious imprint on such a scalar representation of the magnetic field.

In Figures 8 and 9, we show magnetic energy and helicity spectra along with the corresponding transfer spectra at the last time in the simulation. While in the helical case (Run E), $kH(k, t)/2$ is almost equal to $E(k, t)$ for k values near the position of the spectral magnetic energy peak, it is about 10 times weaker in the nonhelical case (Run A). If time were to continue to grow, the difference between the two lines would decrease further; see Figure 3. The magnetic energy has a clear k^5 subinertial range spectrum and a k^{-3} inertial range spectrum. The helicity spectra are a bit steeper both for $k\xi < 1$ and $k\xi > 1$.
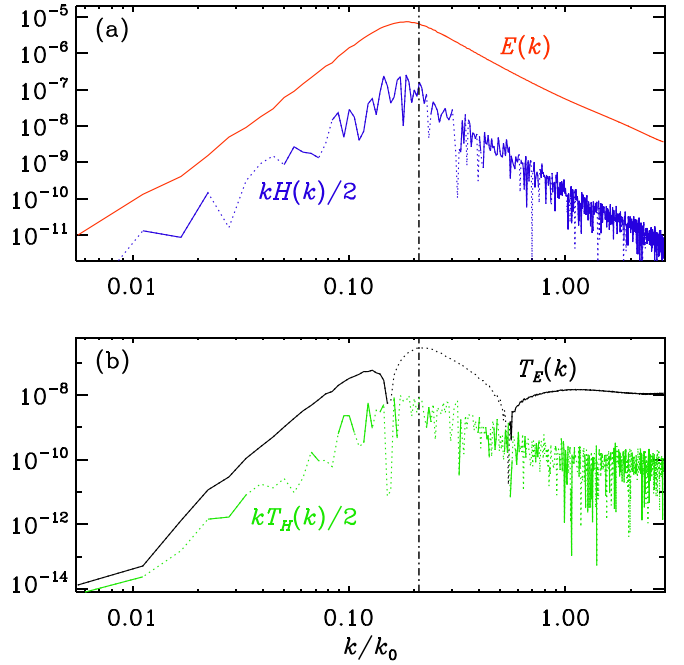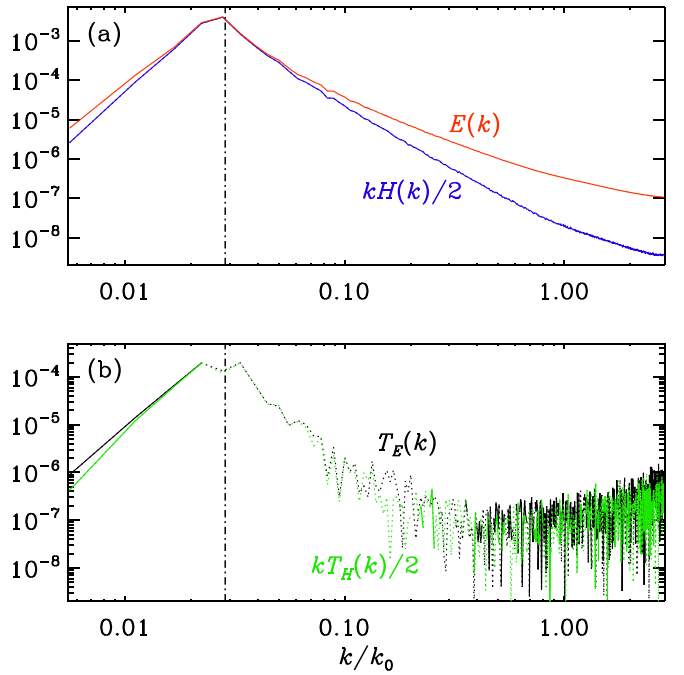
3.5. Fractional Magnetic Helicity

The case of fractional magnetic helicity is arguably the most important case, because there is always some helicity in each hemisphere of any rotating stratified body, and it is usually never 100%. The ratio $\mathcal{H}/2\xi(t)\mathcal{E}$ is between -1 and $+1$ and is a measure of the degree of fractional magnetic helicity. It turns out that, unlike the case of usual MHD (Tevzadze et al. 2012), in the Hall cascade, a very small amount of magnetic helicity
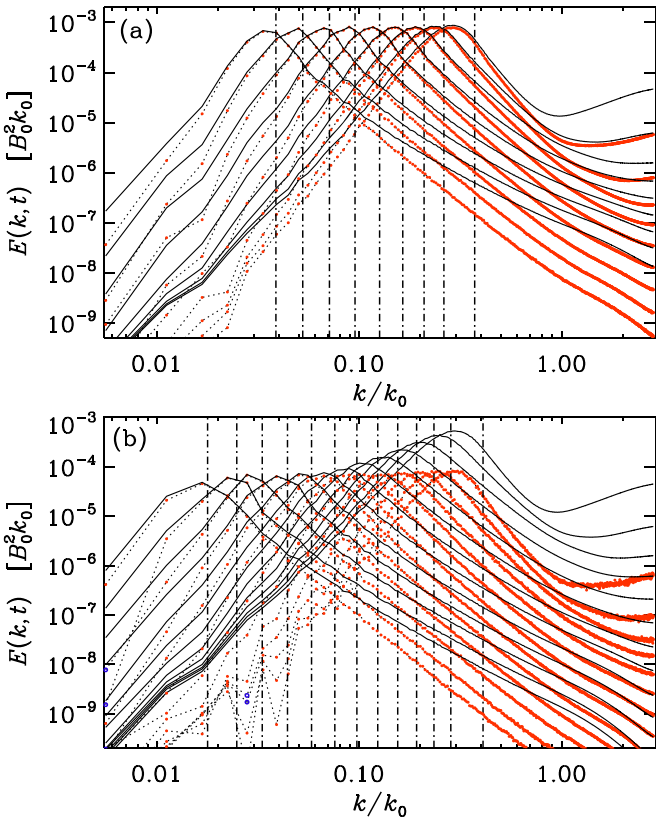
Figure 10. Similar to Figure 2, but for Runs D and C and fractional initial magnetic helicity with (a) $\sigma = 10^{-2}$, and (b) $\sigma = 10^{-3}$.

($\sigma = 10^{-3}$) can lead to nearly 100% helicity in a moderate amount of time; see Figure 10.

The consequences of the realizability condition become apparent when comparing energy and helicity spectra at subsequent times in the same plot; see Figure 10. We see that the normalized helicity spectrum quickly begins to evolve underneath a flat envelope (with no or a very small slope).

The spectral magnetic energy is initially much larger than $kH(k, t)/2$, because the fractional helicity is small. Rather soon, however, the magnetic energy spectrum reaches $kH(k)/2$ and cannot drop any further. By that time, the fractional magnetic helicity has reached nearly 100% at $k \approx \xi^{-1}$. Both at smaller and larger k, however, the magnetic field cannot reach 100%, presumably because of a direct cascade of current helicity for $k\xi \gg 1$, as in ordinary MHD (Brandenburg & Subramanian 2005). A current helicity cascade makes $k^2H(k)$ nearly parallel to $E(k)$, so $kH(k)/2$, which is what is plotted, falls off faster than $E(k)$. Also, for $k\xi \ll 1$, the $kH(k)/2$ spectrum is steeper than that of $E(k)$, and it even changes sign. Looking at Figure 9, however, we see that the difference between $kH(k)/2$ and $E(k)$ is much less for $k\xi \ll 1$ than for $k\xi \gg 1$, so the steeper slope of $kH(k)/2$ for $k\xi \ll 1$ may not be significant.

To illustrate the effect of the realizability condition, we recall that, dividing Equation (29) by k and integrating over k, we obtain

$$2\xi\mathcal{E} \equiv 2\int k^{-1}E(k, t)\,dk \geqslant \int |H(k, t)|\,dk \geqslant |\mathcal{H}|. \quad (31)$$

In Table 4 we list the four terms for Runs A–C and E at some selected times, where we have denoted the penultimate term by $\tilde{\mathcal{H}} \equiv \int |H(k, t)|\,dk$. For the nonhelical runs (A and B), we find
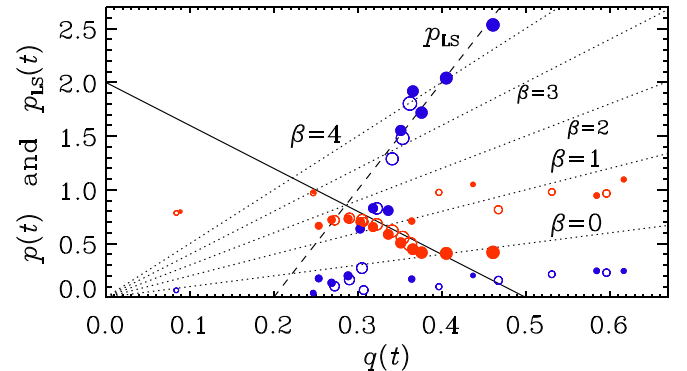

Figure 11. Similar to Figure 4, but for Runs C (for filled symbols) and C' (for open symbols).

Table 4
Examples Illustrating the Realizability Condition for Runs A–C and E at Selected Times

Run	$t\eta_0 k_0^2$	$\mathcal{E}/\mathcal{E}_0$	$k_0\xi$	$2\xi\mathcal{E}/\mathcal{H}_0$	$\tilde{\mathcal{H}}/\mathcal{H}_0$	$|\mathcal{H}|/\mathcal{H}_0$
A	0.4	1.0000	1.9	298.49	1.30	1.00
	1.7	0.3537	2.8	157.51	0.96	0.78
	17	0.0513	4.8	39.24	0.54	0.52
	170	0.0062	8.6	8.59	0.33	0.32
	1700	0.0007	16.0	1.89	0.18	0.18
	8100	0.0002	24.1	0.70	0.11	0.11
B	0.17	1.000	2.5	150.82	1.17	1.00
	1.7	0.192	5.2	61.19	0.95	0.90
	17	0.032	9.9	19.70	0.82	0.80
	170	0.005	19.4	6.54	0.70	0.70
	810	0.002	30.7	3.08	0.65	0.65
C	0.17	1.0000	2.4	7.95	1.00	1.00
	1.7	0.1956	5.2	3.31	0.90	0.90
	17	0.0378	10.3	1.26	0.81	0.81
	170	0.0107	22.7	0.79	0.73	0.73
	1700	0.0041	56.4	0.76	0.68	0.68
E	0.0017	1.0000	1.1	1.06	1.00	1.00
	0.017	0.5207	2.2	1.08	1.02	1.02
	0.17	0.1981	5.7	1.05	1.01	1.01
	1.7	0.0785	14.1	1.04	0.98	0.98
	17	0.0313	35.1	1.03	0.97	0.97

Note. $\mathcal{E}_0$ and $\mathcal{H}_0$ denote the initial values of $\mathcal{E}$ and $\mathcal{H}$, respectively.

$\tilde{\mathcal{H}} > |\mathcal{H}|$ at early times, but even Run C with fractional magnetic helicity obeys $\tilde{\mathcal{H}} = |\mathcal{H}|$ already at early times. At late times, the fractional helicity, $\mathcal{H}/2\xi\mathcal{E}$, is still only 21% for Run B and 16% for Run A.

The pq diagram in Figure 11 confirms that the point (p, q) evolves along the self-similarity line from $\beta = 2$ toward $\beta = 0$. There is actually still a small separation between the red-filled symbols and the self-similarity line. In this connection, we recall that we used in all of our runs the value $r = 0.43$, although for $\beta \to 0$, the value $r = 0.20$ would have been more appropriate. This is indeed the case; see the open symbols in Figure 11 for Run C'.

3.6. Dissipation

An important outcome of our models is the resulting Joule dissipation. A certain fraction of this energy supply is believed to power the observed X-ray emission of the central compact
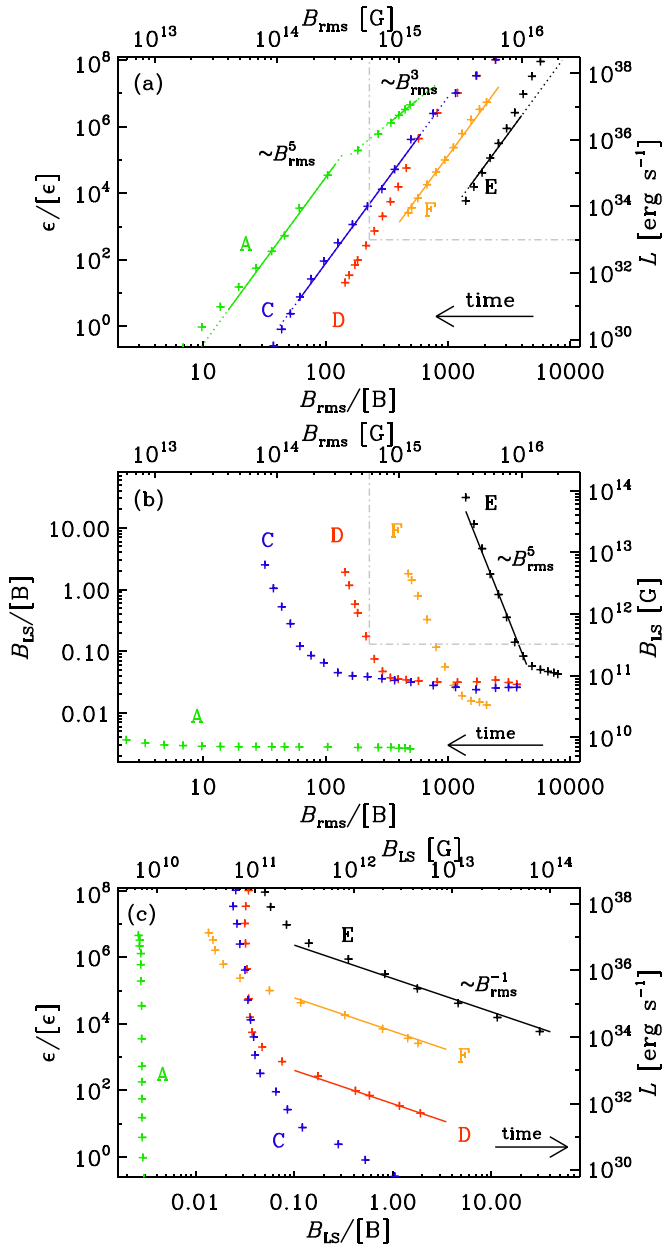
9

Figure 12. (a) Magnetic dissipation and (b) large-scale magnetic field vs. $B_{\rm rms}$ for Runs A (green), C (blue), D (red), E (orange), and F (black). The plus signs denotes different times increasing from right to left, separated by a factor 2.15. The straight lines in (a) and (b) show the $B_{\rm rms}^5$ and $B_{\rm rms}^{-5}$ scalings, respectively, with dotted sections denoting departures from the plus symbols. In (a), we also show the $B_{\rm rms}^3$ scaling for the early phase of Run A.

objects of supernova remnants (Gourgouliatos et al. 2016, 2018, 2020). However, there is also neutrino emission from the crust (Viganò et al. 2013). Therefore, there is no direct equivalence between Joule dissipation and the final X-ray emission, which depends on a number of factors, including the resulting thermal stratification of the crust; see Pons & Viganò (2019) for a review. With this caveat in mind, we must consider the "total" luminosities quoted below as upper limits for the X-ray luminosity.

We have computed the Joule dissipation ϵ from our models as a function of time. As $B_{\rm rms}$ decreases, ϵ also decreases. It is useful to plot ϵ versus $B_{\rm rms}$. The result is shown in Figure 12 for Runs A and C–F. In panel (a), we clearly see that ϵ is a very

steep function of $B_{\rm rms}$. At the same time as $B_{\rm rms}$ decreases, the large-scale field increases. This is shown in panel (b) where we plot $B_{\rm LS} = (2\mathcal{E}_{\rm LS})^{1/2}$ versus $B_{\rm rms}$. These dependencies are also very steep—inversely proportional to be $B_{\rm rms}^5$. Since $\epsilon \propto B_{\rm rms}^5$ and $B_{\rm LS} \propto B_{\rm rms}^{-5}$, we have $\epsilon \propto B_{\rm LS}^{-1}$; see Figure 12(c).

Our work has shown that the magnetic energy and correlation length depend in power-law form on time with $\mathcal{E} \propto t^{-p}$ and $\xi \propto t^q$, respectively, where $p = 6/7$ and $q = 2/7$ in the nonhelical case with $\beta = 2$ and $p = q = 2/5$ in the helical case with $\beta = 0$; see Table 1. Since Joule dissipation is given by $\eta\mu_0 \boldsymbol{J}^2$, we expect $\epsilon \propto \eta\mathcal{E}\xi^{-2}$, and therefore $\epsilon \propto t^{r-p-2q} \propto B_{\rm rms}^s$, with $s = 2(p + 2q - r)/p$. Thus, we have $s = 7/3 \approx 2.33$ in the nonhelical case with $\beta = 2$ and $s = 5$ in the helical case with $p = q = 2/5$.

Most of our results show a dependence compatible with $\epsilon \propto B_{\rm rms}^5$. Run A shows initially a shallower scaling close to $B_{\rm rms}^3$ (which would be expected for $\beta = 1$), although the theoretically expected scaling would be shallower. The scaling of the red line in Figure 12 does perhaps best describe the values proposed by Gourgouliatos et al. (2016, 2020) for their global model of NS crusts with $\ell = 10$. The gray lines in Figure 12 highlight a particular example with a total luminosity $L_{\rm tot} = 10^{33}$ erg s^{-1}, which corresponds to $B_{\rm rms} \approx 6 \times 10^{14}$ G. Thus, we can write

$$L_{\rm tot} = 10^{33}\left(\frac{B_{\rm rms}}{6 \times 10^{14}\,{\rm G}}\right)^5 \text{erg s}^{-1} \quad \text{(red line).} \qquad (32)$$

Figure 12(b) shows that then $B_{\rm LS} \approx 3 \times 10^{11}$ G.

We also see from Figure 12(b) that nonhelical magnetic fields do not produce significant large-scale magnetic fields (see the green curve). However, because those fields decay much more rapidly, they also dissipate more energy for a given field strength. If such a scenario was to be viable, one would need to have a preexisting large-scale magnetic field. This could lead to more rapid magnetic field decay (Brandenburg et al. 2020) and would need to be studied more carefully.

As already emphasized by Gourgouliatos et al. (2020), only the large-scale magnetic field of NSs can be observationally inferred from the spin-down of pulsars. Therefore, we show in Figure 12(c) ϵ versus $B_{\rm LS}$. We see that ϵ now decreases with increasing $B_{\rm LS}$. The slope is -1 for fractionally helical magnetic fields at late times, as expected from the aforementioned quintic scalings of ϵ and $B_{\rm LS}$ with $B_{\rm rms}$.

3.7. Dissipation in the Stratified Case

Real NS crusts are strongly stratified with n_e and η varying over several orders of magnitude. The radial variation of n_e has already been considered by Vainshtein et al. (2000) and Hollerbach & Rüdiger (2004), but they assumed η to be constant. Approximately realistic profiles for both n_e and η were adopted in the works of Pons & Geppert (2007) and Viganò et al. (2013) in two dimensions and Gourgouliatos et al. (2016, 2020) in three dimensions. Here we adopt the prescription of Gourgouliatos et al. (2016, 2020), who used the value $H_e/R = 0.0463$ for the scale height. With $d/R = 0.1$, this corresponds to $k_1 H_e = (2\pi/d)H_e \approx 2.9$.

The resulting profiles of $n_e \propto \zeta(z)$ and $\eta \propto \zeta^{-2/3}$ are shown in Figure 13. For comparison with a stronger and even more realistic stratification, we also include a case with $k_1 H_e = 0.7$. We see that at the surface, we have the values
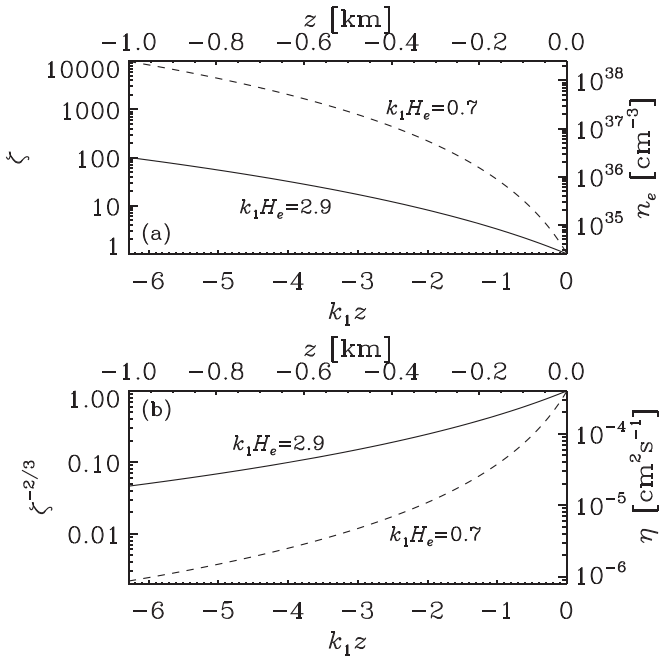
Figure 13. (a) ζ (left axis) and n_e (right axis), and (b) $\zeta^{-2/3}$ (left axis) and η (right axis) vs. $k_1 z$ (lower axes) and z (upper axes) for $k_1 H_e = 2.9$ (solid lines) and $k_1 H_e = 0.7$ (dashed lines).

Table 5
Parameters for the Stratified Models

Run	σ_0	$\phi_0(k_1 z = -6)$	$\phi_0(k_1 z = -3)$	$\phi_0(k_1 z = -1)$
Bz	0	0.0007	⋯	0.0070
Cz	0.001	0.006	0.012	0.043
Dz	0.01	0.06	0.12	0.30
Ez	1	⋯	⋯	⋯
CZ	0.001	0.0003	0.0033	0.013
z	$\xi_0 \rightarrow$	0.003	0.005	0.009
Z	$\xi_0 \rightarrow$	0.001	0.002	0.005

Note. Dashes indicate that a fit would be uncertain. The resolution is 1024^3.

$n_e = 2.5 \times 10^{34}$ cm^{-3} and $\eta = 4 \times 10^{-4}$ cm^2 s^{-1} that were quoted in Section 2.1 in SI units. These values were also used by Gourgouliatos et al. (2016, 2020), where the surface conductivity was $\sigma_{\rm el} = 1.8 \times 10^{23}$ s^{-1}. This value is similar to that of Pons & Geppert (2007), who give surface values for $\sigma_{\rm el}$ of around 10^{23} s^{-1} for temperatures of slightly below 10^8 K, and somewhat larger values for smaller temperatures. This conductivity corresponds to $\eta = c^2/4\pi\sigma_{\rm el} = 7 \times 10^{-4}$ cm^2 s^{-1} in cgs units, where $c = 3 \times 10^{10}$ cm s^{-1} is the speed of light. In the strongly stratified case with $k_1 H_e = 0.7$, n_e and η vary between top and bottom of the domain by four and nearly three orders of magnitude, respectively. The latter variation is similar to that in Figure 1 of Pons & Geppert (2007).

We then solve Equation (4) with nonperiodic boundary conditions in the z direction. We have calculated models for different values of the initial helicity parameter σ_0; see Table 5 for Runs Bz–Ez, which have the same values of σ_0 as the unstratified counterparts, Runs B–E. We also list Run CZ, which has $k_1 H_e = 0.7$ and $\sigma = 0.001$ (like Runs C and Cz). As before, we use $k_0/k_1 = 180$ in all stratified cases.
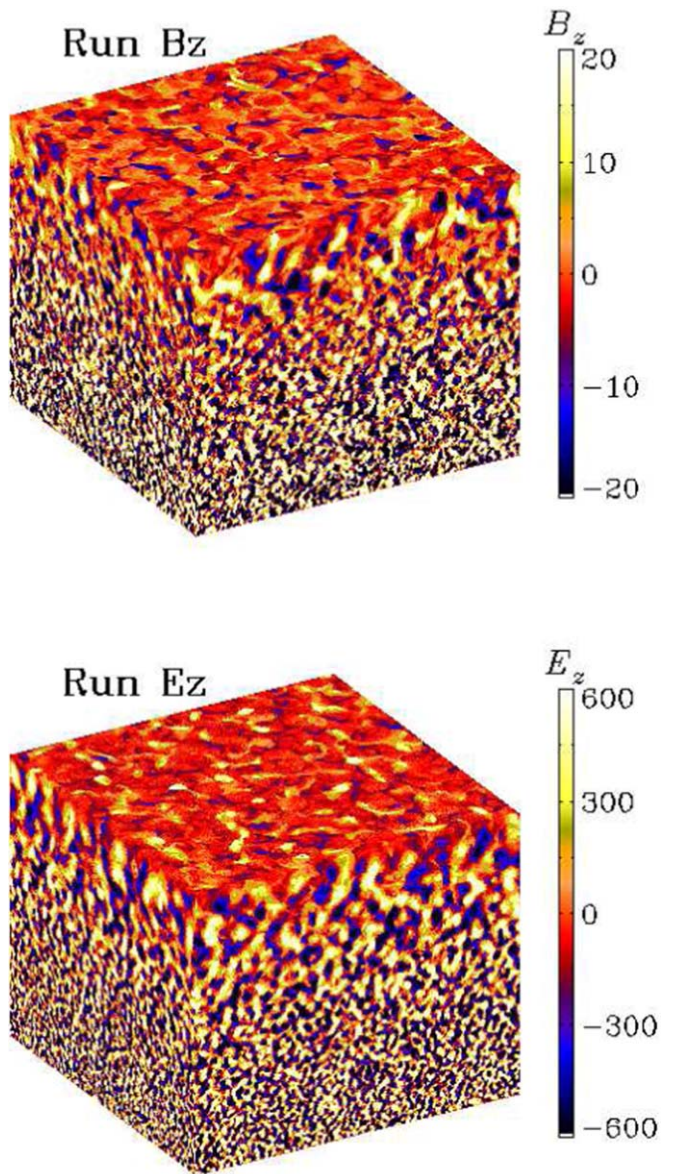

Figure 14. Similar to Figure 7, but for Runs Bz and Ez.

In Figure 14 we show B_z for Runs Bz and Ez at times $\eta_0 k_0^2 t = 80$ and 3.5, respectively, which is when the correlation lengths are comparable in the two runs. We see that the magnetic structures have larger length scales in the upper layers. This is primarily a consequence of the larger magnetic diffusivity there. In the fully helical case (Run Ez), the formation of larger length scales is accelerated by the presence of magnetic helicity.

To determine the fractional magnetic helicity as a function of z and t, we now employ a method that does not require Fourier transformation. The relevant information is contained in the ratio

$$\overline{\boldsymbol{A} \cdot \boldsymbol{B}}/\overline{\boldsymbol{B}^2} \equiv \phi\xi, \qquad (33)$$

where $\phi(z, t)$ is the fractional magnetic helicity, $\xi(z, t)$ is a suitability defined correlation length, and overbars denote xy averaging. Instead of using Equation (16), which requires
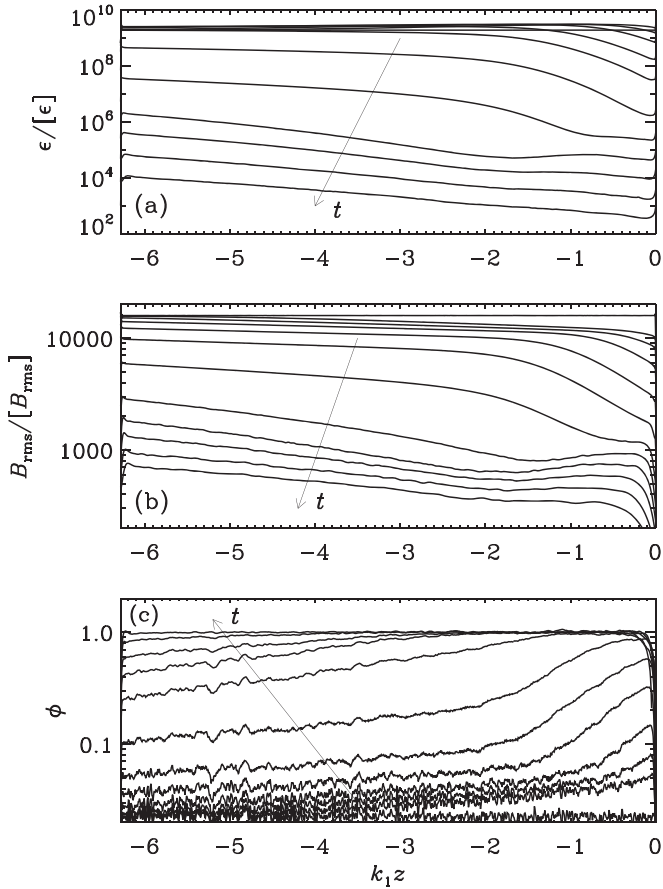
Figure 15. (a) Dissipation, (b) rms magnetic field, and (c) fractional magnetic helicity vs. height for Run Dz for increasing times, as indicated by the arrows, in steps of $10^{1/2} \approx 3.2$ until $\eta_0 k_0^2 t = 140$.

Fourier transformation, we compute ξ from the ratio

$$\xi^2 = \overline{\boldsymbol{A} \cdot \boldsymbol{B}} / \overline{\boldsymbol{J} \cdot \boldsymbol{B}}. \tag{34}$$

It is then convenient to determine ϕ from the quantity

$$\phi^2 = \overline{\boldsymbol{A} \cdot \boldsymbol{B}} \; \overline{\boldsymbol{J} \cdot \boldsymbol{B}} / (\overline{\boldsymbol{B}^2})^2. \tag{35}$$

For very small fractional helicities, however, ϕ^2 can occasionally become negative in some places. In all other cases, however, it is possible to compute $\phi(z, t)$.

In Figure 15, we plot the z dependence of ϵ, B_{rms}, and ϕ at different times. It turns out that ϵ is largest in the deeper parts. This is mainly a consequence of B_{rms} having decayed most rapidly near the surface, where η is large. We also see from Figure 15(c) that ϕ grows fastest in the upper layers.

To study the growth of ϕ in more detail, we compare in Figure 16 the time dependence for Runs Bz–Dz and CZ for three values of z. It turns out that, in an intermediate range, ϕ grows approximately algebraically like

$$\phi(z, t) = \phi_0(z)(t/t_0)^{2/3}, \tag{36}$$

where t_0 was defined in Equation (20). The values of $\phi_0(z)$ are listed in Table 5 for $k_1 z = -6$, -3, and -1. The magnetic helicity production in the initially nonhelical Run B is a result of random fluctuations and could equally well have been of the opposite sign. In that case, ϕ^2 would normally still be positive, because the sign of magnetic helicity affects the signs of both $\overline{\boldsymbol{A} \cdot \boldsymbol{B}}$ and $\overline{\boldsymbol{J} \cdot \boldsymbol{B}}$. The square root of their ratio gives ξ and is
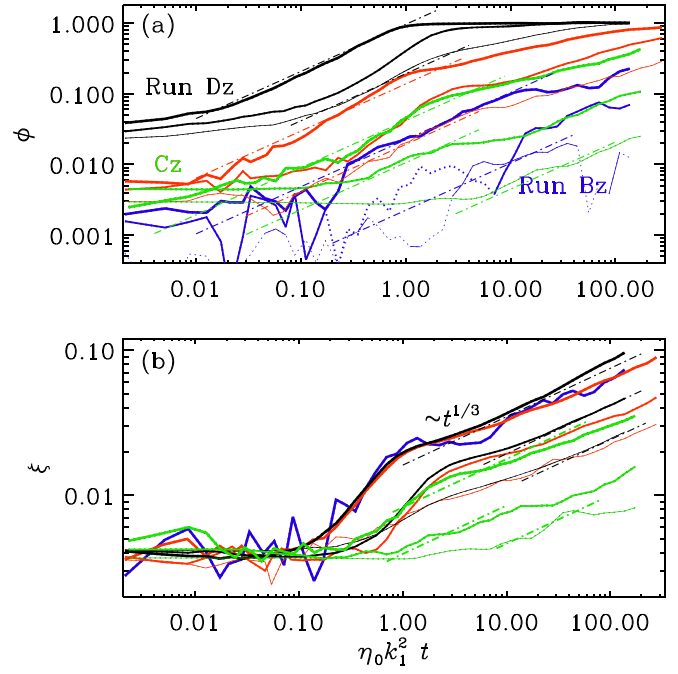

Figure 16. (a) $\phi(t)$ for Runs Bz (blue), Cz (red), Dz (back), and CZ (green) at $k_1 z = -6$, -3, and -1, as indicated by the increasing line thickness. Dotted lines fragments indicate $|\phi|$ when ϕ is negative. The dashed–dotted lines indicate the fits with the $\phi_0(z)$ given in Table 5. (b) $\xi(t)$ for $k_1 z = -1$ for Runs Bz–Dz and CZ.
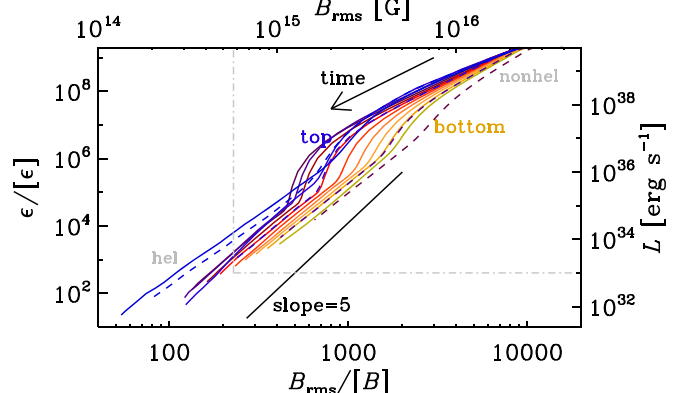

Figure 17. Similar to Figure 12(a), but for Run Cz (solid lines) and Run CZ (dashed lines), showing the dependencies separately for each horizontal layer, except for Run CZ, where only the surface layers with comparable values of ζ are plotted. Yellow (blue) shades indicate locations near the bottom (top) of the domain.

shown in the lower panel of Figure 16. It also obeys power-law scaling of the form

$$\xi(z, t) = \xi_0(z)(t/t_0)^{1/3}, \tag{37}$$

where the $\xi_0(z)$ are similar for all three runs, suggesting that their values are approximately independent of the magnetic helicity for fixed stratification. The $\xi_0(z)$ increase with z; see the last two lines of Table 5 for models of series z and Z with $k_1 H_e = 2.9$ and 0.7, respectively.

An important question is how the dissipation properties in the cases with stratification compare with the unstratified cases. We therefore show again a parametric representation of ϵ versus B_{rms}, but now for each horizontal layer separately. The result is shown in Figure 17. Interestingly, the different curves

tend to collapse on top of each other. Furthermore, we obtain a similar $\epsilon \propto B_{\rm rms}^5$ scaling as in the unstratified case, but it is now along two branches that are slightly offset relative to each other. The upper branch is somewhat shallower ($\epsilon \propto B_{\rm rms}^3$). Nevertheless, the values of ϵ and $B_{\rm rms}$ are remarkably similar to those in the unstratified cases, and are again compatible with $L \approx 10^{33}$ erg s^{-1} for a $B_{\rm rms}$ of a few times 10^{14} G. This can be seen by comparing with the gray dashed–dotted lines in Figure 12, which have also been reproduced in Figure 17 at the same position.

The relatively good agreement between Figures 12(a) and 17 provides some justification for using the unstratified models as a meaningful local representation of the Hall cascade in NS crusts. The reason why unstratified models were previously found to yield a poor representation of the case with stratification (Pons & Geppert 2010) is probably related to the fact that those authors studied a large-scale nonturbulent magnetic field, which is more sensitive to boundary conditions.

The sudden drop in ϵ for intermediate $B_{\rm rms}$ is probably caused by the gradual transition from a fractionally helical to a fully helical magnetic field, which occurs here not only as a function of time, but also as a function of z. Near the surface, as already shown in Figure 16, this transition happens earlier than in the deeper parts.

The work of Gourgouliatos et al. (2016, 2020) only considered the case of moderately strong stratification, where $k_1 H_e = 2.9$. In addition to possible numerical problems, there is always the general difficulty for stronger stratification (smaller values of $k_1 H_e$) that the characteristic timescales in the problem become very different between top and bottom of the domain. The time step is limited mainly by the Hall nonlinearity in the surface layers, but the evolution in the deeper layers becomes very slow, so we need a large number of time steps to describe the full time evolution.

4. Conclusions

The present work has confirmed that the Hall cascade can liberate a significant amount of dissipative energy through Joule heating. The resulting heating is proportional to $B_{\rm rms}^5$ for helical and fractionally helical magnetic fields. The magnetic fields undergo strong inverse cascading with a temporal decay significantly slower ($\propto t^{-2/5}$) than in MHD ($\propto t^{-2/3}$). However, even in the nonhelical cases, there can be inverse cascading, but only for strong magnetic fields.

We confirmed the $k^{-7/3}$ inertial range spectrum both in forced and decaying cases. The nondimensional coefficient $C_{\rm Hall}$ in this relation has been determined to be approximately 1.6 in the helical case and 2.7 in the nonhelical case. However, this was not a major focus of attention and more accurate determinations should be performed using dedicated higher resolution simulations. The current helicity cascade, expected to be proportional to k^{-2}, is also worth reconsidering. Furthermore, in the decaying case, we find a steeper subinertial range spectrum proportional to k^5. It develops independently of the subinertial range slope of the initial field.

Most of our models predict a rather sensitive dependence of the heating rate on the magnetic field strength proportional to the fifth power of the rms value. It would be useful to confirm the generality of this scaling using global models such as those used by Gourgouliatos et al. (2016, 2018, 2020). These steep dependencies can potentially be employed as sensitive diagnostic tools that may give us information about the dominant physical processes leading to the X-ray emission for the central compact objects of supernova remnants of different ages. Before doing this, however, it would be necessary to establish the detailed connection between Joule dissipation and X-ray luminosity and to determine the contribution from neutrino emission.

The inverse cascade in the helical case has been seen before (Cho 2011), but it was analyzed only at a qualitative level. We quantified this here by plotting the exponent $p_{\rm LS}$ as a function of q, which we find to be compatible with a linear relation. For the helical case, we find $p_{\rm LS} \approx 2$, which implies an approximately quadratic growth of the large-scale field with time. The existence of such a relation was not anticipated. However, our phenomenological scaling relation tends to predict slightly smaller values of $p_{\rm LS}$ in some cases. This could be related to finite size effects that lead to a slightly shallower spectrum at small k and thereby to larger $\mathcal{E}_{\rm LS}$, which could explain the faster growth. How significant this departure is remains unclear, so this too would be worth reconsidering.

The mechanism for inverse cascading in the nonhelical case is not very clear either. It is possible that magnetic helicity fluctuations could be responsible for this. The usual fractional magnetic helicity is clearly too small, but even the value based on the modulus of the magnetic helicity spectrum, $\tilde{\mathcal{H}} = \int |H(k, t)| \, dk$, is small and is equal to $|\mathcal{H}|$ at late times; see Table 4. Therefore, this explanation might not be fully satisfactory.

At late times, our simulations display a self-similar decay. We have seen that the correlation length ξ increases by a factor of around 100 by the end of our simulations; see Figure 10(b). For later times, one would need to allow for the finite extent of the global spherical shell geometry of NS crusts, as was already done by Gourgouliatos et al. (2016, 2018, 2020). They considered the peak of the spectral magnetic energy to be at a spherical harmonic degree of around $\ell = 10$–20, which corresponds to "effective" values of k_0 that are already comparable to k_1, the smallest vertical wavenumber in our domain. We must therefore regard our local simulations as the early stages of a self-similar evolution, after which the finite shell geometry is best described by global models with $\ell \sim R/\xi$.

Most of our attention went into the study of local unstratified models with periodic boundary conditions. However, it turns out that much of the physics of the unstratified models can be recovered in the stratified ones with nonperiodic boundaries at the appropriate depth. It will be interesting to see whether this similarity between stratified and unstratified models persists also when studying models where the local temperature evolution is taken into account. Technically, this should well be feasible with the PENCIL CODE. In this connection, we remind the reader that both the code and the input files are freely available. It would also be useful to couple the present studies to models of the very early phases of NSs. One would then be able to relax the assumption of an initial magnetic field that was here assumed to have the same rms value at all heights. It should be emphasized, however, that the earlier onset of growth of magnetic helicity in the upper layers of our models is not connected with our choice of the initial condition and is just a consequence of η being larger near the surface.

Software and Data Availability. The source code used for the simulations of this study, the Pencil Code (Brandenburg & Dobler 2010), is freely available on https://github.com/pencil-code/. The DOI of the code is https://doi.org/10.5281/zenodo.3961647 (Brandenburg 2020b). The simulation setup and the corresponding data are freely available on https://doi.org/10.5281/zenodo.3951873 (Brandenburg 2020a).

ORCID iDs

Axel Brandenburg ⬤ https://orcid.org/0000-0002-7304-021X

References

Batchelor, G. K., & Proudman, I. 1956, RSPTA, 248, 369
Biskamp, D., & Müller, W.-C. 1999, PhRvL, 83, 2195
Biskamp, D., Schwarz, E., & Drake, J. F. 1996, PhRvL, 76, 1264
Biskamp, D., Schwarz, E., Zeiler, A., Celani, A., & Drake, J. F. 1999, PhPl, 6, 751
Brandenburg, A., Durrer, R., Huang, Y., et al. 2020, PhRvD, 102, 023536
Brandenburg, A. 2020a, Datasets for "Hall cascade with fractional magnetic helicity in neutron star crusts," v2020.07.20, Zenodo, 10.5281/zenodo.3951873
Brandenburg, A. 2020b, Pencil Code, v2020.08.06, Zenodo, 10.5281/zenodo.3961647
Brandenburg, A., & Dobler, W. 2010, Pencil Code, Astrophysics Source Code Library, ascl:1010.060
Brandenburg, A., & Kahniashvili, T. 2017, PhRvL, 118, 055102
Brandenburg, A., Kahniashvili, T., Mandal, S., et al. 2017, PhRvD, 96, 123528
Brandenburg, A., Kahniashvili, T., & Tevzadze, A. G. 2015, PhRvL, 114, 075001
Brandenburg, A., & Nordlund, Å. 2011, RPPh, 74, 046901
Brandenburg, A., & Subramanian, K. 2005, A&A, 439, 835
Chamel, N., & Haensel, P. 2008, LRR, 11, 10
Cho, J. 2011, PhRvL, 106, 191104
Cho, J., & Lazarian, A. 2004, ApJL, 615, L41
Cho, J., & Lazarian, A. 2009, ApJ, 701, 236
Durrer, R., & Caprini, C. 2003, JCAP, 0311, 010
Epstein, R. I. 1979, MNRAS, 188, 305
Goldreich, P., & Reisenegger, A. 1992, ApJ, 395, 250
Gourgouliatos, K. N., Hollerbach, R., & Archibald, R. F. 2018, A&G, 59, 5.37
Gourgouliatos, K. N., Hollerbach, R., & Igoshev, A. P. 2020, MNRAS, 495, 1692
Gourgouliatos, K. N., Wood, T. S., & Hollerbach, R. 2016, PNAS, 113, 3944
Hollerbach, R., & Rüdiger, G. 2002, MNRAS, 337, 216
Hollerbach, R., & Rüdiger, G. 2004, MNRAS, 347, 1273
Olesen, P. 1997, PhLB, 398, 321
Pons, J. A., & Geppert, U. 2007, A&A, 470, 303
Pons, J. A., & Geppert, U. 2010, A&A, 513, L12
Pons, J. A., & Viganò, D. 2019, LRCA, 5, 3
Rempel, M. 2014, ApJ, 789, 132
Rheinhardt, M., & Geppert, U. 2002, PhRvL, 88, 101103
Saffman, P. G. 1967, PhFl, 10, 1349
Tevzadze, A. G., Kisslinger, L., Brandenburg, A., & Kahniashvili, T. 2012, ApJ, 759, 54
Thompson, C., & Duncan, R. C. 1993, ApJ, 408, 194
Vainshtein, S. I., Chitre, S. M., & Olinto, A. 2000, PhRvE, 61, 4422
Viganò, D., Rea, N., Pons, J. A., et al. 2013, MNRAS, 434, 123
Wareing, C. J., & Hollerbach, R. 2009, PhPl, 16, 042307
Wareing, C. J., & Hollerbach, R. 2010, JPlPh, 76, 117